SIAM J. LIFE SCIENCES
Vol. 1, No. 1, pp. 1–29

Dynamic Homeostasis in Relaxation and Bursting Oscillations*

Christopher J. Ryzowicz†, Richard Bertram†‡§, and Bhargav R. Karamched‡§¶

Abstract. Homeostasis traditionally describes the regulation of a stable internal state despite external perturbations, but many biological systems are intrinsically dynamic, exhibiting oscillations across multiple timescales. In this work, we introduce a theoretical framework for dynamic homeostasis (or homeodynamics) in systems with fast-slow dynamics, showing that the temporal average of a slow variable can remain robust under parameter changes, even when fast variables oscillate wildly. We first apply this to the FitzHugh–Nagumo model to illustrate relaxation oscillations, and then extend to models of electrical bursting and calcium oscillations in pancreatic β-cells. In bursting models with multiple slow components, only the variable driving the current bursting regime demonstrates homeostatic invariance. Our results highlight that homeostasis can manifest in the averaged behavior of slow variables, rather than in fast oscillatory dynamics, suggesting a new way to understand regulatory stability in excitable biological systems.

Relevance to Life Sciences. Homeostasis, broadly speaking, refers to the maintenance of a stable internal state when faced with external or internal stimuli. Failure to manage these regulatory processes can lead to different diseases or death. Most physiologists and cell biologists around the world agree that homeostasis is a fundamental tenet of their disciplines. Nevertheless, a precise definition of homeostasis is hard to come by. Often times, homeostasis is simply defined as "you know it when you see it."

Mathematical Content. Mathematical treatments of homeostasis involve studying equilibria of dynamical systems that are relatively invariant with respect to parameters. However, physiological processes are rarely static and often involve dynamic processes such as oscillations. In such dynamic environments, quantities such as average values may be relatively invariant with respect to parameters. This has been referred to as "homeodynamics." We present a general framework for homeodynamics involving systems with two or more timescales that elicits homeostasis in the temporal average of a species. The key point is that homeostasis manifests when measuring the slow variable responsible for driving oscillations and is not apparent in the fast variables. We demonstrate this in the FitzHugh–Nagumo model for relaxation oscillations and then in two models for electrical bursting activity and calcium oscillations in pancreatic β-cells. One of these models has multiple slow variables, each driving the bursting oscillations in different parameter regimes, but homeodynamics is only present in the variable currently engaged in this role.

Key words. relaxation oscillations, Fitzhugh–Nagumo, fast-slow analysis, bursting, homeostasis

MSC codes. 92B25, 37N25

DOI. 10.1137/25M1779309

*Received by the editors July 18, 2025; accepted for publication (in revised form) October 13, 2025; published electronically March 30, 2026.

https://doi.org/10.1137/25M1779309

†Department of Mathematics, Florida State University, Tallahassee, FL 32306 USA (cjr22@fsu.edu, rbertram@fsu.edu).

‡Institute of Molecular Biophysics, Florida State University, Tallahassee, FL 32306 USA.

§Program in Neuroscience, Florida State University, Tallahassee, FL 32306 USA.

¶Corresponding author. Department of Mathematics, Florida State University, Tallahassee, FL 32306 USA (bkaramched@fsu.edu).

1. Introduction. A central question in physiology and cell biology is how various systems maintain homeostasis. Homeostasis is identified as one of the key tenets of physiology and biology by many top researchers around the world [1, 35]. Surprisingly, its precise definition and the biomolecular control systems that facilitate it remain an open question [36].

Why is homeostasis important? Broadly speaking, homeostasis refers to the maintenance of a stable internal state even when faced with (potentially drastic) external or internal disturbances. Homeostatic conditions in humans typically include a core body temperature of 98.6°F (37°C), blood glucose levels around 85 mg/dL (4.7 mmol/L), and a slightly basic blood pH of about 7.4. Failure to regulate processes so that such values are maintained in a multitude of environments can lead to severe disorders or death [23].

To understand homeostasis, physiologists and cell biologists have adopted the theory and vernacular of control systems—thereby framing complicated biophysical networks with a mathematical lens. Mathematically, homeostasis can be interpreted as a circumstance wherein the equilibrium of a dynamical system is relatively invariant with respect to alterations to the system parameters. Indeed, Reed, Golubitsky, and others published a series of papers that investigate various biomolecular control systems to determine what network motifs facilitate homeostasis [15, 20, 39, 40, 41]. An example of a network motif facilitating homeostasis is feedback inhibition:

$$I \xrightarrow{+} X \xrightarrow{+} Y \xrightarrow{+} Z \xrightarrow{-} Y.$$

In this example, the input, I, feeds into a pathway that amplifies biochemical species X. This leads to the eventual production of biochemical species Z, which inhibits the production of Y. In Figure 1, we show the equilibrium value of Z as I is varied. The curve resembles a chair, with the "seat" of the chair occurring over the interval of I values for which the equilibrium

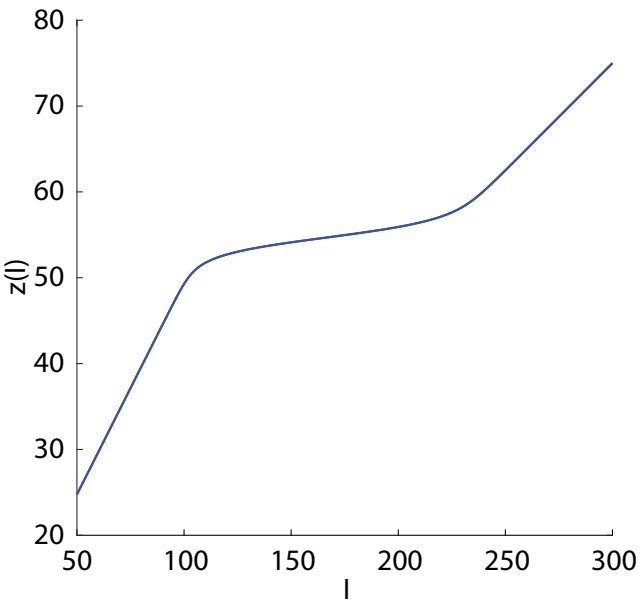

Figure 1. *Homeostatic chair curve of equilibria z as a function of the input values I.*

Z values are relatively invariant, which we refer to as semi-invariant. This semi-invariance is representative of homeostasis.

Golubitsky, Stewart, and others have developed rigorous mathematical theory characterizing the conditions under which a system exhibits homeostasis [16, 20, 21, 22, 55]. The basic idea is that homeostasis occurs when the derivative of an output with respect to the input is zero. To precisely characterize homeostasis, they invoke singularity theory.

A limitation of these characterizations of homeostasis is the focus on equilibria. Many physiological observables exhibit rich dynamical profiles such as oscillations, bursting [5, 28, 42], or even chaos [30]. Quantities commonly associated with static equilibrium values, such as body temperature or blood glucose levels, actually oscillate [2, 51, 56]. This suggests that more complicated temporal signatures, not just static equilibria, may encode homeostasis.

In this paper, we propose a general framework for a novel physiological architecture of homeostasis. We focus on excitable systems with multiple timescales that undergo bifurcations to limit cycles. For some input values, such systems will rapidly contract to a stable equilibrium. However, the equilibrium can destabilize via, for example, a Hopf bifurcation or homoclinic bifurcation. With multiple timescales, the resulting oscillation will manifest as a relaxation oscillation characterized by a slow build-up process followed by fast transitions [8]. Such relaxation oscillations are observed in biological rhythms of calcium [49], voltage [37], and cardiac dynamics [19].

We show that homeostasis is observed in relaxation oscillations when looking at the temporal average of the oscillatory signals. In particular, the temporal average of the slow variable exhibits homeostasis—the fast variable fails to exhibit homeostasis. The underlying reason for this is that the trajectory of the limit cycle in phase space is semi-invariant with respect to input parameters. Specifically, the slow variable oscillates back and forth as a sawtooth wave between the same values for all oscillation-facilitating input values. Thus, its temporal average does not change. The fast variable appears as a square wave that jumps between the same values for all inputs in the oscillatory regime; however, the proportion of the period the oscillation spends in the ON phase (i.e., the duty cycle) of the time signal varies, thereby yielding different temporal averages. We thus show how a complicated temporal signal may encode homeostasis and establish which variables to measure to detect it. Dynamic homeostasis is a term used when combining the idea of homeostasis with physiological processes that oscillate [31, 56]. Our mechanism for detecting homeostasis is one among potentially many that may fall under this general phenomenon.

We first demonstrate this phenomenon in the FitzHugh–Nagumo model. We further show that including noise in the input allows for the relaxation oscillator to work even better as an encoder of homeostasis. We then generalize our findings to a biologically relevant bursting oscillation using both a deterministic and a stochastic version of the Chay–Keizer model for pancreatic β-cells [12]. Thereafter, we briefly look at a system with multiple slow timescales [9] to show how homeostasis may be observed in systems with multiple slow variables.

2. Relaxation oscillations with the FitzHugh–Nagumo model.

The FitzHugh–Nagumo (FHN) model is a simple, 2-dimensional model, adapted from the van der Pol oscillator [54]. Introduced by FitzHugh [17] in 1961 and refined by Nagumo et al. (see [38]) a year later, the model is also a simplified version of the 4-dimensional Hodgkin–Huxley equations for neuronal

spiking [27]. It replicates many neuronal phenomena from the Hodgkin–Huxley equations but is easier to analyze due to its lower dimensionality.

2.1. Excitability and relaxation oscillations in the FHN model. We begin by reviewing two fundamental features of the FHN model: excitability and oscillations. The nondimensional model satisfies the ordinary differential equations

$$\frac{dx}{dt} = \mu\left(x - \frac{x^3}{3} - y\right), \qquad \frac{dy}{dt} = \frac{1}{\mu}(J + \alpha x - y), \tag{1}$$

where $x(t)$ and $y(t)$ are the activator variable (analogous to the membrane potential) and the recovery variable (analogous to a K^+ channel gating variable), respectively [18]. The parameter $\alpha > 0$ controls the strength of coupling feedback, and the parameter $\mu \gg 1$ controls the timescale separation (we use $\mu = 30$ in all simulations). We consider the case in which the recovery variable is modulated by an input parameter J that could reflect gene expression of the ion channels responsible for spike repolarization.

The equilibria of the FHN model are obtained by setting both temporal derivatives in equations (1) equal to zero. This results in the following algebraic equations for the equilibria (x^*, y^*):

$$\frac{x^{*3}}{3} + (\alpha - 1)x^* + J = 0, \qquad y^* = J + \alpha x^*.$$

For $\alpha \geq 1$ the system admits one real equilibrium. If the input parameter J satisfies either $J < \frac{2}{3} - \alpha$ or $J > \alpha - \frac{2}{3}$, the equilibrium will be locally stable (see Appendix A for linearization and stability analysis). Figures 2(A)–(B) depict the possible dynamics of this system when the equilibrium is stable and μ is sufficiently large. The stable node (filled black circle) occurs at the intersection of the x-nullcline (black cubic curve) and the y-nullcline (gray line). If we impart a small perturbation away from the equilibrium in one direction (black star), a subthreshold response occurs. That is, the system passively converges back to equilibrium. However, if we impart a perturbation in a different direction (black square), a superthreshold response occurs. The trajectory undergoes a "spike" before converging back to equilibrium. The threshold between these two different behaviors is the middle branch of the cubic x-nullcline. This threshold phenomenon, called excitability, is the defining feature of a model for impulse generation.

When $J \approx \pm(\frac{2}{3} - \alpha)$, the system undergoes a subcritical Hopf bifurcation (see Appendix A for Hopf bifurcation analysis), rendering the equilibrium unstable for $\frac{2}{3} - \alpha < J < \alpha - \frac{2}{3}$ and causing the onset of periodic solutions (see Figure 2(C)). These emergent periodic solutions are unstable but quickly change stability and grow in amplitude to become relaxation oscillations that are characterized by a substantial timescale separation between the state variable dynamics due to the choice of the parameter μ (Figure 2(D)). In this model, x evolves on a fast timescale and y evolves on a slower timescale. See [8] for a discussion of relaxation oscillations.

2.2. Slow variable time-average shows semi-invariance, fast variable does not. For the remainder of the paper we focus primarily on persistent oscillations, starting with relaxation oscillations produced by the FHN model. Examples of two relaxation oscillations, with $J = 0$

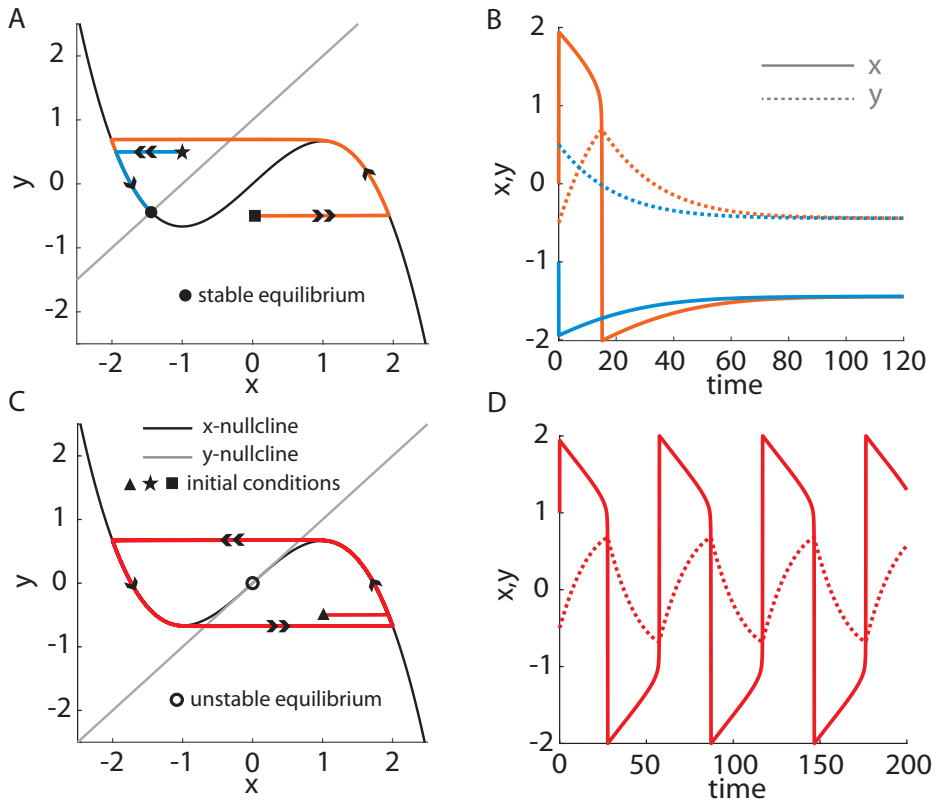

Figure 2. *Dynamics of system* (1) *for* $\alpha = 1$, $\mu = 30$, *and* (A)–(B) $J = 1$ *or* (C)–(D) $J = 0$. *Left column: Dynamics in the* (x, y)*-plane with* x*-nullcline (black),* y*-nullcline (gray), and sample trajectories (color). The blue curves indicate subthreshold responses to perturbation from rest, while the orange curves indicate superthreshold responses. The double arrows indicate fast motion, while the single arrows indicate slower motion. The filled circle is a stable equilibrium; the open circle is an unstable equilibrium. Right column: Time series of the trajectories from the* (x, y)*-plane on the left showing* (B) *subthreshold and superthreshold responses, and* (D) *relaxation oscillations.*

and $J = 0.8$, are shown in Figure 3. Increasing J from 0 to 0.8 results in an upward translation of the y-nullcline, shifting the equilibrium closer to the lower knee of the cubic x-nullcline (Figure 3(A)). This change has almost no effect on the limit cycle; the limit cycles for the two values of J lie almost directly on top of each other in phase space. The time series for y has a sawtooth shape for both values of J (Figure 3(B)). Although the limit cycle is almost unchanged by the change in J, the period is somewhat different, so the y oscillations drift apart over time. In spite of this, the time-average of y, $\langle y \rangle$, is almost identical for the two values of the input.

To determine the extent of the semi-invariance, we simulated the FHN model and computed $\langle y \rangle$ over a range $J \in [-3, 3]$ increasing by increments of 0.05. The result is shown in Figure 4(A). For small values of J, below the threshold for oscillations, increasing the input causes a substantial increase in $\langle y \rangle$. For large values of J, above the threshold for oscillations, increasing the input also causes a substantial increase in $\langle y \rangle$. For intermediate values of J,

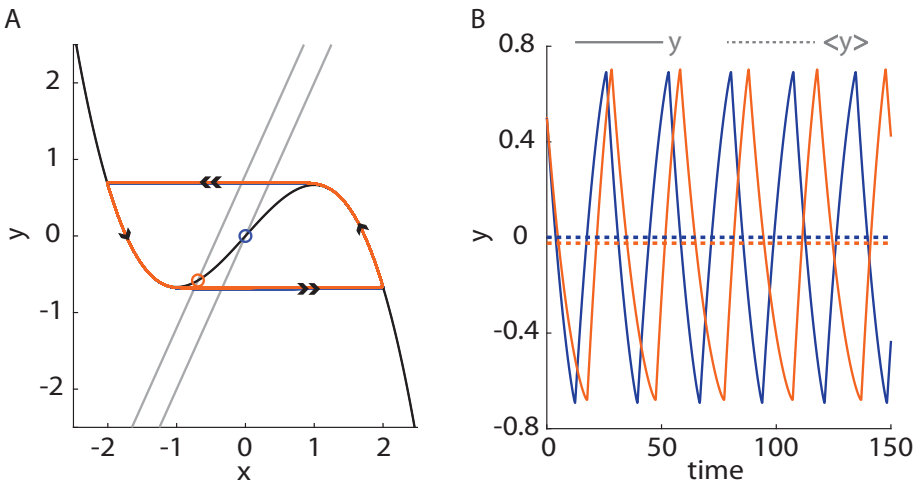

Figure 3. *Semi-invariance in the mean of the slow variable with changes in the input.* (A) *Phase portrait for the cases $J = 0$ (blue) and $J = 0.8$ (orange). Increasing J translates the y-nullcline (gray lines) upward and leaves the x-nullcline (black curve) unchanged. This results in a left shift in the equilibrium, but no change in stability (open circles). Limit cycles for the two cases (colored curves) are almost identical.* (B) *Time series for y in the two cases (solid curves) and the time-average values (dashed lines) show semi-invariance of the mean value of the slow variable. For both cases, $\alpha = 2$.*

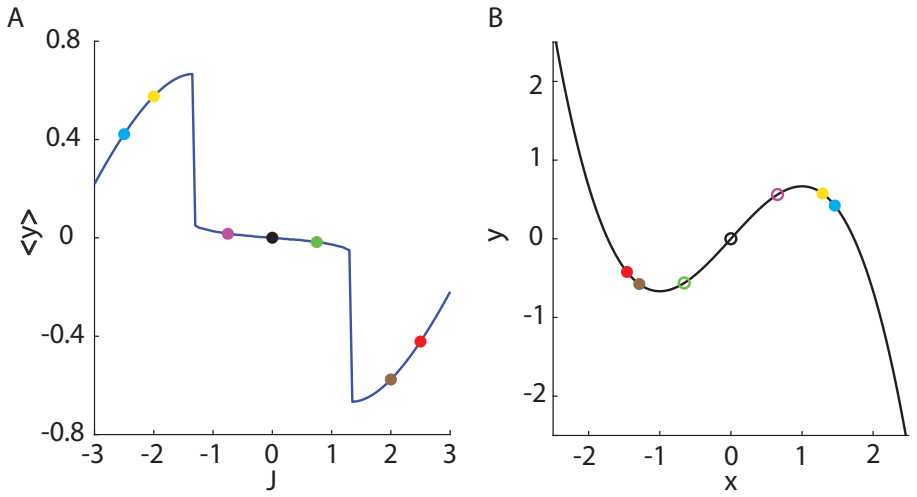

Figure 4. *Dynamic homeostasis in the time-average of the slow variable of the FHN model.* (A) *Homeostatic chair over a range of input values $J \in [-3, 3]$ with $\alpha = 2$.* (B) *Phase space showing the x-nullcline (black curve) and colored points indicating the locations of equilibria with different J values. The equilibria are color coded to correspond with the colored points in panel* A.

however, changes in the input lead to very little change in $\langle y \rangle$. This semi-invariance in $\langle y \rangle$ is an example of dynamic homeostasis [31, 50, 56, 57]. This phenomenon results in a "homeostatic chair" curve similar to Figure 1 and described in prior studies [15, 20, 39, 40, 41]. The key difference, however, is that in those models the homeostasis is in the value of a variable at

equilibrium. In our case, it is in the average value of a variable over an oscillation period, or dynamic homeostasis. As shown in Figure 4, semi-invariance in the variables at equilibrium does not occur in the FHN model.

The dynamic homeostatic plateau section (the "seat") of the chair curve exists in the same parameter range of J in which the relaxation oscillations occur. Figure 4(B) shows phase space with the x-nullcline (black curve) and seven points that indicate different equilibria for distinct values of J. The corresponding $\langle y \rangle$ values are shown in Figure 4(A) in matching colors. The three points on the seat (magenta, black, and green) correspond to the points which lie in between the two knees of the x-nullcline. These are locations where the equilibrium is unstable and oscillations occur as seen in Figure 3(A). Outside of this range, the equilibria are locally stable (red, brown, yellow, and cyan) and the system does not oscillate.

This observation, that the semi-invariant portion of the chair corresponds to the parameter interval in which there are relaxation oscillations, also explains the two large jumps in the chair curve. At a small value of J there is a stable equilibrium with a large y value (either the yellow or cyan point in Figure 4). For a somewhat larger J value for which the stable equilibrium is replaced by a stable periodic solution (magenta point), y reaches down to negative values during the oscillation, yielding a $\langle y \rangle$ value much smaller than when the equilibrium was stable. Thus, there is a sudden jump down in the left portion of the chair curve, at $J \approx -1.33$. At the other extreme, when J is positive and just past 1, the transition from periodic solutions (green point) covering both positive and negative y values to a stable equilibrium with a negative y value (brown point), results in a large decrease in $\langle y \rangle$. This is the second jump down, in the right portion of the chair curve at $J \approx 1.33$.

2.2.1. There is no invariance in the time-average of the fast variable. We next consider how the time-average of the fast variable x, $\langle x \rangle$, changes with changes in J. This is plotted as a function of J in Figure 5(A). As with the slow variable, there is no invariance in this variable over intervals of J where the equilibrium is stable. Unlike before, however, there is no invariance in $\langle x \rangle$ over intermediate values of the input (approximately $-1.33 < J < 1.33$). The reason for this is evident in the x time series (Figure 5(B)), using two values of J within the oscillation region (orange and black points in Figure 5(A)). With the lower input value, the duty cycle (the duration of an "up phase" versus the entire oscillation period) is higher than with the higher input value. As a result, the time-average value of x is higher with the lower input (dashed orange line) than with the higher input (dashed black line). The change in the duty cycle, which is responsible for the lack of invariance in $\langle x \rangle$, occurs because J changes the proximity of the y-nullcline (gray curve in Figure 3(A)) to the left and right branches of the x-nullcline (black curve in Figure 3(A)). At a higher value of J the y-nullcline is closer to the left branch of the x-nullcline than it is when J is lower, so the speed of the trajectory along that branch is slower. As a result, when J is larger there will be a longer "down state" (and a shorter "up state") in the x oscillations, yielding a lower duty cycle. The central point here is that biological relaxation oscillations can exhibit dynamic homeostasis in the mean, but only in the slow variable.

2.3. The homeostatic range depends on the feedback strength. The feedback strength, α, affects the slope of the y-nullcline, but has no effect on the x-nullcline of the FHN model. In particular, increasing α increases the slope of the y-nullcline (Figure 6(A)). What effect

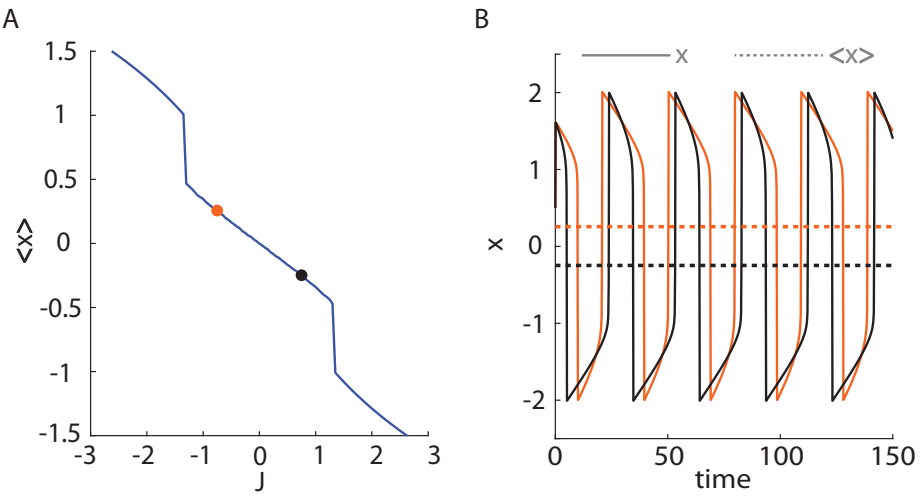

Figure 5. *Lack of dynamic homeostasis in the fast variable dynamics of the FHN model.* (A) *The time-average of x plotted as a function of input J shows no homeostasis.* (B) *The time series for two values of J (solid curves) and time-averages (dashed lines) show a substantial difference in $\langle x \rangle$ due to the difference in the oscillation duty cycle. For both panels, $\alpha = 2$.*

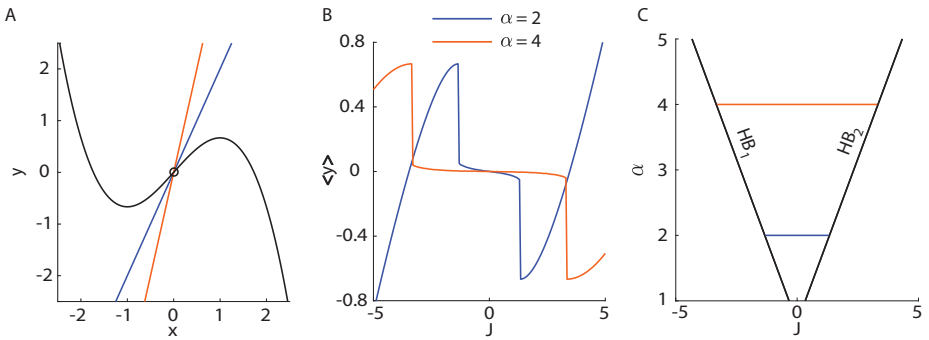

Figure 6. *Semi-invariance depends on the feedback strength.* (A) *Phase plane when $\alpha = 2$ (blue) and $\alpha = 4$ (orange). The y-nullcline slope increases with α, while x-nullcline (black curve) remains unchanged.* (B) *Homeostatic chair curves of $\langle y \rangle$ as a function of J when $\alpha = 2$ (blue) and $\alpha = 4$ (orange).* (C) *Two-parameter bifurcation diagram in (J, α)-space with Hopf bifurcation solutions (black curves).*

does this have on the interval of dynamic homeostasis? To answer this question we simulated the FHN model over a wide range of J values and determined the asymptotic time-average of the slow variable for different α values. When α is increased from 2 (blue) to 4 (orange), the range of J values at which there is dynamic homeostasis increases (Figure 6(B)).

The reason for the lengthening of the homeostatic interval can be explained by the effect of α on the location of the Hopf bifurcations that initiate and terminate the relaxation oscillations. In Figure 6(C) we plot a two-parameter bifurcation diagram of the Hopf bifurcations in the (J, α)-space (see Appendix A for Hopf bifurcation analysis). The branches of the loci of Hopf bifurcation points (black) are approximately linear. The range of J values in which there is a homeostatic plateau in $\langle y \rangle$ is approximately the range of values of J between the Hopf

bifurcation branches. Thus, we conclude that the homeostatic region grows approximately linearly as α increases.

2.4. Input stochasticity extends the range of homeodynamics in the FHN model. Biological systems, especially at the intracellular level, operate in crowded, heterogeneous, noisy environments [11, 29, 32, 53]. Hence, it is important to develop biological models that incorporate stochasticity and analyze its effects on the dynamics. In this section, we analyze the effects of stochasticity in input on the homeostasis property of the FHN model.

The modified differential equations are

$$\frac{dx}{dt} = \mu\left(x - \frac{x^3}{3} - y\right), \qquad \frac{dy}{dt} = \frac{1}{\mu}(J^* + \alpha x - y), \tag{2}$$

where all parameters and variables are defined as in (1), except the input stimulus J^* is a normally distributed random variable

$$J^* \sim N(J, \sigma), \tag{3}$$

where J is the mean of the normal distribution and σ is the standard deviation (strength of the noise).

We numerically solved (2) using the forward Euler method, randomly assigning the input stimulus every integral time step according to (3). We then calculated the time-average of the slow variable, $\langle y \rangle$, after sufficiently long time for many different values of the normal distribution mean, J. The time-average as a function of J for different standard deviations ($\sigma = 0, 10, 20, 30$) is given in Figure 7(A). For very small and very large values of J, increasing (decreasing) the mean input results in an increase (decrease) in $\langle y \rangle$ regardless of the standard deviation. However, for intermediate values of J, the effects of changing J on $\langle y \rangle$ depend on the standard deviation of the distribution. We quantified these changes in two different ways: (1) measuring the slopes of the seats of the chair curves, and (2) measuring the length of the oscillation interval in terms of J.

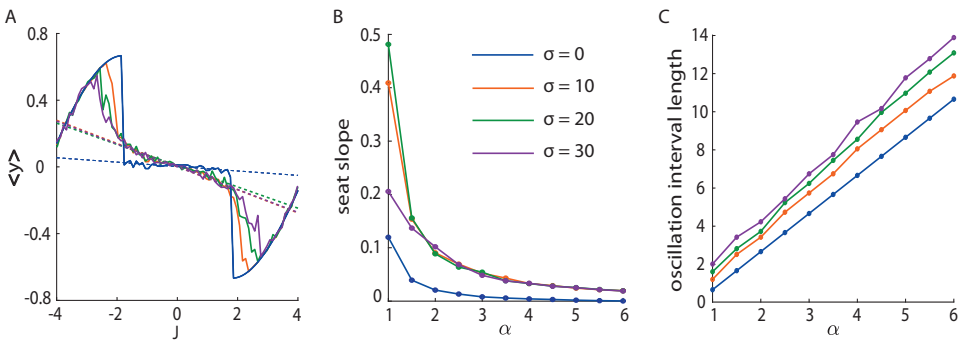

Figure 7. *Dynamic homeostasis is preserved when stochasticity is added to the input stimulus of the FHN model.* (A) *Homeostatic chair curve for the deterministic model ($\sigma = 0$) and stochastic models ($\sigma = 10, 20, 30$). Linear regression (dashed lines) show trends within the seat portion of the chair. A feedback strength of $\alpha = 2.5$ was used for the simulations.* (B) *The seat slope declines with α in both the deterministic and stochastic models.* (C) *The range of J values for which the FHN model exhibits oscillations increases with α for both the deterministic and stochastic models.*

Dynamic homeostasis can be characterized as a segment of the $\langle y \rangle$ versus J curve that is flat, or has a slope near 0. This segment is like the seat of the chair, so we refer to it as the "seat slope." To determine the effects of noise in the input, we computed the seat slope for different values of the noise strength σ using linear regression on the $\langle y \rangle$ values over the interval of J between the two Hopf bifurcation values of the deterministic model (i.e., when $\sigma = 0$). This was repeated for different values of α, the parameter that sets the slope of the y-nullcline. The seat slope as a function of α is plotted in Figure 7(B). One observation is that the slope for the deterministic curve is less than that of all of the stochastic curves regardless of the α value. This is because the noise skews the chair curves near the ends of the seat (e.g., Figure 7(A) near $J \approx \pm 2$). It is also evident that the seat slopes of the stochastic model become very similar for all values of σ as α increases. For low α values, the difference in slope values between the stochastic and deterministic curves is large because the distances between the Hopf bifurcations are small (see Figures 6(B)–(C)). That is, the seat intervals are short. For larger α values, the seat slopes of the stochastic simulations not only converge to one another, but also approach those of the deterministic model. These numerical results show that dynamic homeostasis is largely preserved when noise is added to the input stimulus.

Although stochasticity in the input increases the seat slope, thereby somewhat degrading the homeostasis in $\langle y \rangle$, it also extends the range of J values for which oscillations are produced, and in this way extends the interval of dynamic homeostasis. This occurs because, with stochastic input J, even when the mean J is outside of the oscillation interval for the deterministic model, J values from within the oscillation interval are still sampled. As a result, while the deterministic model would be at a stable equilibrium state, the model with stochastic input, but the same mean value of J, exhibits irregular oscillations and thereby extends the homeostatic range.

To quantify the extent to which the seat of the homeostasis curve was extended by the stochastic input, we computed the difference, for each J, between a stochastic chair curve in Figure 7(A) and the deterministic curve. Specifically, we looked for values of J that pulled the stochastic chair curve away from the equilibrium branch of the deterministic chair curve. Once that difference was sufficiently large ($\Delta = 0.03$), we used that J value as an end point for the oscillation interval. This was done for each end point, and the distance between these two end points is plotted in Figure 7(C) as the "oscillation interval length." For each value of the feedback strength α the oscillation interval length is longer for the model with stochastic input than for the deterministic model. Indeed, the greater the noise strength, the greater the extension of the oscillation interval.

3. Bursting oscillations with the Chay–Keizer model. Chay and Keizer published the first biophysical model for bursting electrical activity and Ca^{2+} oscillations in pancreatic β-cells in the early 1980s [12], following the experimental work of Atwater et al. [4]. This model, along with models for electrical bursting in neurons, was used in pioneering work on the analysis of bursting oscillations by decomposing the system into fast and slow subsystems (see [42, 44]). This fast-slow analysis technique would be used in subsequent studies of bursting oscillators [5, 8, 10, 45]. In this section, we use the Chay–Keizer model and fast-slow analysis to demonstrate dynamic homeostasis in the slow variable that drives bursting oscillations.

3.1. Model formulation. In the original form [12], the Chay–Keizer model is 5-dimensional with differential equations for the membrane potential (V), two activation variables, one inactivation variable, and the free intracellular Ca^{2+} concentration (c). However the important dynamics are preserved with a 3-dimensional reduction consisting of dynamics of V, the fraction of open K^+ channels (w), and c. The reduced model [6] is

$$\frac{dV}{dt} = -(I_{Ca} + I_K + I_{K(Ca)} + I_{K(ATP)} - I_{ap})/C_m, \tag{4}$$

$$\frac{dw}{dt} = \frac{w_\infty(V) - w}{\tau_w}, \tag{5}$$

$$\frac{dc}{dt} = -f(\beta I_{Ca} + k_c c). \tag{6}$$

The dynamics of V (4) are governed by the different ionic currents and by the membrane capacitance C_m. The parameter I_{ap} is the applied external current or a background current. The first term (I_{Ca}) is the inward Ca^{2+} current that depolarizes the membrane and produces the upstroke of an action potential or spike. Its activation is fast, and it is assumed to change instantaneously with V. The second term (I_K) is the outward delayed rectifier K^+ current, responsible for the downstroke of the action potential. Its activation occurs on a slower timescale ($\tau_w = 16$ ms), and its dynamics are characterized by (5). The currents are given by

$$I_{Ca} = g_{Ca} m_\infty(V)(V - V_{Ca}),$$
$$I_K = g_K w(V - V_K),$$

where g_{Ca} and g_K are maximum conductance parameters, m_∞ is the equilibrium value for the fraction of open Ca^{2+} channels, and w is the fraction of open delayed rectifying K^+ channels. The constants V_{Ca} and V_K are the calcium and potassium reversal potentials, respectively. The equilibrium activation functions are V-dependent Boltzmann functions:

$$m_\infty(V) = \frac{1}{1 + \exp\left(\frac{v_m - V}{s_m}\right)},$$
$$w_\infty(V) = \frac{1}{1 + \exp\left(\frac{v_w - V}{s_w}\right)},$$

where v_m and v_w are parameters that set the half-maximum response, and s_m and s_w set the slope of the activation curve.

The third term ($I_{K(Ca)}$) in (4) describes the ionic current through Ca^{2+}-activated K^+ channels in which the gating is determined by intracellular Ca^{2+}. The fraction of activated K(Ca) channels is described by a Hill function that increases with c, and the ionic current is given by

$$I_{K(Ca)} = g_{K(Ca)} \left(\frac{c^p}{K_\Omega^p + c^p}\right)(V - V_K),$$

where $g_{K(Ca)}$ is the maximum conductance parameter, p is the Hill coefficient, and the parameter K_Ω sets the intracellular Ca^{2+} concentration for half-maximum activation of the channels.

Table 1

Parameter values used in all figures for the Chay–Keizer model, except k_c which is varied in several figures.

Parameter	Value	Parameter	Value
g_{Ca}	1200 pS	I_{ap}	500 mV
$g_{K(Ca)}$	300 pS	p	5
g_K	3000 pS	K_Ω	0.3 μM
$g_{K(ATP)}$	230 pS	τ_w	16 ms
C_m	5300 fF	β	$2.25 \times 10^{-6}\mu$M fA^{-1} ms^{-1}
v_w	-16 mV	s_w	5 mV
v_m	-20 mV	s_m	12 mV
V_K	-75 mV	f	0.001
V_{Ca}	25 mV	k_c	0.07 ms^{-1}

The fourth term ($I_{K(ATP)}$) in (4) is the adenosine triphosphate (ATP)-sensitive K^+ current. Assuming constant conductance, the current satisfies

$$I_{K(ATP)} = g_{K(ATP)}(V - V_K),$$

where $g_{K(ATP)}$ is the conductance parameter.

The dynamics of c (6) are characterized by the net flux of Ca^{2+} across the membrane multiplied by f, the fraction of intracellular Ca^{2+} that is free or unbound by buffers. The first term reflects Ca^{2+} influx through Ca^{2+} ion channels, so it is proportional to I_{Ca}. The second term reflects Ca^{2+} removal through Ca^{2+} pumps in the cell's membrane, and is assumed to be directly proportional to c. The parameter β converts current to flux, and the parameter k_c is the Ca^{2+} pump rate.

3.2. Bursting oscillations and fast-slow analysis of the reduced Chay–Keizer model.

The reduced Chay–Keizer model produces electrical bursting with the parameter values listed in Table 1. Each burst is composed of an active phase of spiking and a silent phase where the membrane is hyperpolarized, shown in blue in Figure 8. At the beginning of an active phase, the Ca^{2+} concentration c builds up due to influx from voltage-dependent Ca^{2+} channels. The rise in Ca^{2+} activates K(Ca) current which terminates the spiking and ends a burst active phase. The cell then enters a silent phase where there is a net removal of Ca^{2+} by Ca^{2+} pumps in the membrane. The Ca^{2+} concentration and the K(Ca) conductance are slowly reduced. Once the K(Ca) conductance is sufficiently small, the membrane potential reaches spike threshold again, terminating the silent phase and starting a new active phase.

The fast-slow analysis of this bursting pattern relies on the slow dynamics of c relative to the dynamics of the other two variables, V and w, which form the fast subsystem. A full description of the asymptotic dynamics of the fast subsystem over a range of c values is shown in the bifurcation diagram in Figure 9(A), with c as the bifurcation parameter. This is the "critical manifold" of the fast-slow system. Importantly, the fast subsystem exhibits bistability for values of c between the leftmost saddle-node bifurcation (left green triangle) and the homoclinic bifurcation (green diamond), where both the periodic spiking solutions and low-V equilibrium are stable.

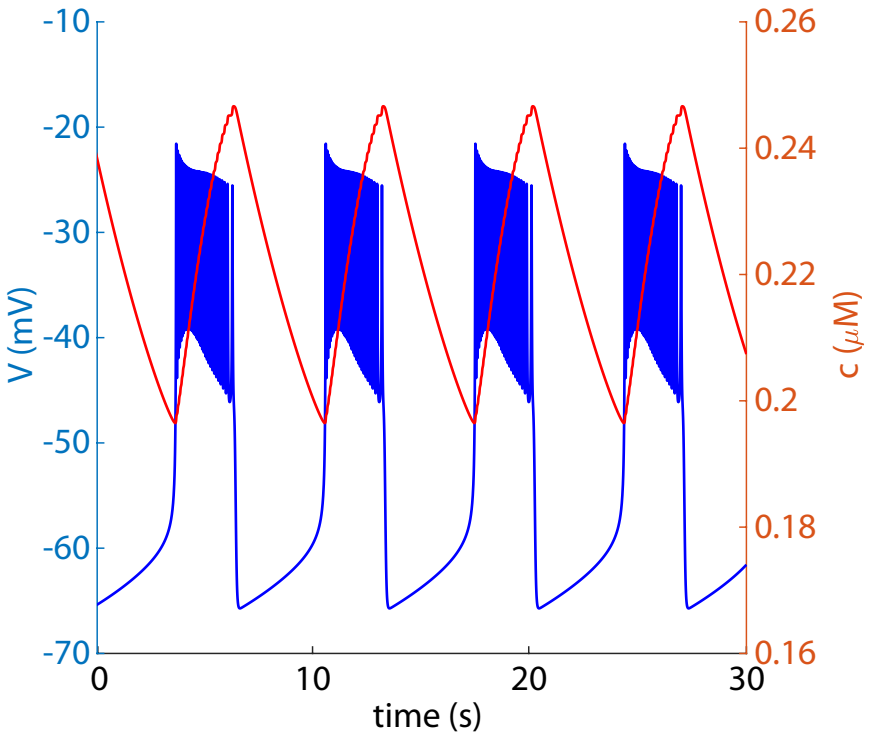

Figure 8. *Bursting oscillations produced by the reduced Chay–Keizer model. Bursting in membrane potential V (blue curve), consisting of active phases where the cell is spiking and silent phases where the cell is hyperpolarized. The intracellular Ca^{2+} concentration c (orange curve) has a slow sawtooth oscillation pattern, rising during the active phase and falling during the silent phase.*

In Figure 9(B) we superimpose the c-nullcline (green curve) and the critical manifold in the (c, V)-plane. The intersection of the critical manifold and the c-nullcline (black open circle) is the equilibrium point of the full 3-dimensional model. Treating the critical manifold as a generalized V-nullcline, we use this and the c-nullcline to determine the flow of a trajectory in the (c,V)-plane, taking into account movement in the c direction is much slower than movement in the V direction due to the timescale separation. A burst trajectory, superimposed in blue, can be understood in terms of flow similar to the relaxation oscillation in Figure 2. During the silent phase, the trajectory slowly tracks along the bottom of the critical manifold until it reaches the left saddle-node or fold. After crossing this, the trajectory jumps up to the stable periodic (spiking) branch. Because in doing so the trajectory crosses the c-nullcline, it now flows to the right. The trajectory continues the spiking pattern while slowly moving rightward until it reaches the homoclinic bifurcation point. From here it jumps down to the stable stationary branch and switches direction to the left to begin a new silent phase.

3.3. Dynamic homeostasis in the time-averaged calcium concentration. We simulated the reduced Chay–Keizer model using (4)–(6) with different values for the Ca^{2+} pump rate (k_c). This is the parameter that is set by the glucose concentration; the pump rate is higher at a higher glucose concentration. We then calculated the asymptotic time-average of the slow

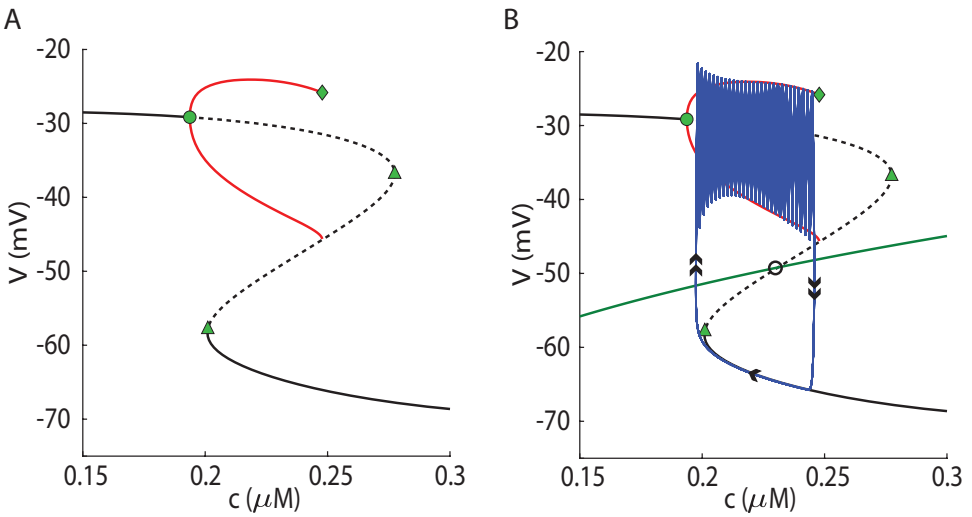

Figure 9. *Fast-slow analysis of the reduced Chay–Keizer model.* (A) *Bifurcation diagram of the fast subsystem. Stable (solid) and unstable (dashed) stationary equilibria are in black. The minimum and maximum V of the stable periodic solutions are in red. There exist a supercritical Hopf bifurcation (green circle), two saddle-node bifurcations (green triangles), and a homoclinic bifurcation (green diamond).* (B) *The c-nullcline (green), full system equilibrium (black open circle), and burst trajectory (blue) are superimposed with the bifurcation diagram from panel* (A)*, now treated as a generalized V-nullcline.*

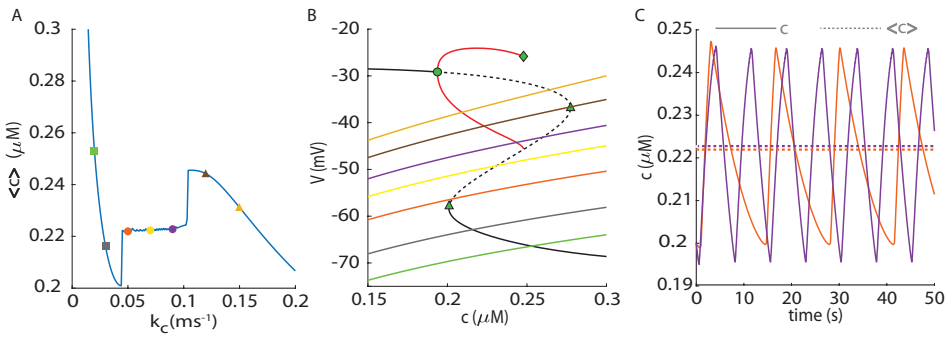

Figure 10. *Dynamic homeostasis in the time-average of the Ca^{2+} concentration in the reduced Chay–Keizer model.* (A) *A homeostatic chair curve is evident over a range of Ca^{2+} pump rate values.* (B) *Critical manifold and c nullcline for several vales of k_c, color coded to match points in panel* (A). (C) *Time series (solid) and time-averages (dashed lines) with $k_c = 0.05\ ms^{-1}$ (orange) and $k_c = 0.09\ ms^{-1}$ (purple) show semi-invariance in the mean Ca^{2+} concentration at equilibrium.*

variable, $\langle c \rangle$, with other parameters taken from Table 1 (see Figure 10(A)). For very small or large values of k_c, increasing (decreasing) the pump rate results in a decrease (increase) in $\langle c \rangle$. Biologically, this makes sense because increasing (decreasing) the pump rate would increase (decrease) how much Ca^{2+} is pumped out of a cell. However, for intermediate values of k_c, changes in this pump rate result in very little change in the time-average of c. Thus, there are dynamic homeostasis and a chair-like curve for a bursting oscillator similar to the one in the previous section for a relaxation oscillator.

The seat of the chair curve in Figure 10(A) exists in the same parameter range of k_c in which bursting oscillations occur. Figure 10(B) shows the critical manifold, which does not change with k_c, and the c-nullcline, which does depend on k_c. These c-nullclines are color coded to correspond to the k_c values at the points in Figure 10(A). As k_c is increased, the c-nullcline shifts upward.

The chair curve can be partitioned into three sections that correspond to the three different asymptotic states of the model. For low values of k_c (squares), the c-nullcline intersects the critical manifold on a stable stationary branch of the fast subsystem (Figure 10(B)). The full-system equilibrium at the intersection of these two curves is locally stable. Therefore, the membrane potential is characterized as fully quiescent at a low value of V. In this silent state, increasing the Ca^{2+} pump rate lowers the mean Ca^{2+} concentration, as can be seen in both panels (A) and (B).

For intermediate values of k_c (circles), the c-nullclines intersect the critical manifold at an unstable equilibrium point of the fast subsystem, so the full-system equilibrium is unstable. Also, in this parameter range the full system produces bursting oscillations, with dynamics similar to Figure 9(B). The time series for c with k_c set to 0.05 ms^{-1} (orange) and 0.09 ms^{-1} (purple) are shown in Figure 10(C). The asymptotic time-averages of c are superimposed as dashed horizontal lines. It is clear that the time-averages of the Ca^{2+} concentration are nearly identical between the two time series, despite the oscillations having different duty cycles and periods. This semi-invariance occurs because the trajectory must cycle between the left saddle-node and homoclinic bifurcations of the critical manifold during each burst cycle, regardless of the oscillation period, and these bifurcations (and the entire critical manifold) are unaffected by k_c.

For higher values of k_c (triangles), the c-nullcline intersects deep within the periodic branch of the critical manifold with the full system equilibrium remaining unstable. However, the trajectory no longer switches between the bottom stationary branch and periodic branch of the generalized V-nullcline to produce bursting. Instead, it gets trapped within the periodic branch and the membrane potential continuously spikes [52]. Because the trajectory no longer cycles between the left saddle-node and homoclinic bifurcation, the invariance is lost, and the mean Ca^{2+} concentration declines with larger values of the pump rate k_c.

3.3.1. The time-average of a fast variable is not homeostatic in a bursting oscillator.

We showed earlier that the time-average of the fast variable x in the FHN model for relaxation oscillations is not homeostatic. To determine whether this is the case for a fast variable in the reduced Chay–Keizer model for bursting, we computed the time-average of the membrane potential, since this would be an observable variable in a β-cell (the other fast variable, w, cannot be directly measured). The time-average membrane potential, $\langle V \rangle$, as a function of k_c is plotted in Figure 11(A). Like before, the graph can be partitioned into three different segments corresponding to the three different dynamic states of the system: quiescence (low k_c), bursting (middle k_c), and continuous spiking (high k_c). This shows that the mean membrane potential is not invariant with respect to k_c, as with the fast variable of the relaxation oscillator.

The time series of membrane potential when $k_c = 0.05$ ms^{-1} (orange) and $k_c = 0.09$ ms^{-1} (black) are shown in Figure 11(B). The asymptotic time-averages of the membrane potential are superimposed as dashed lines. The duty cycle is lower for the lower k_c value, driving the

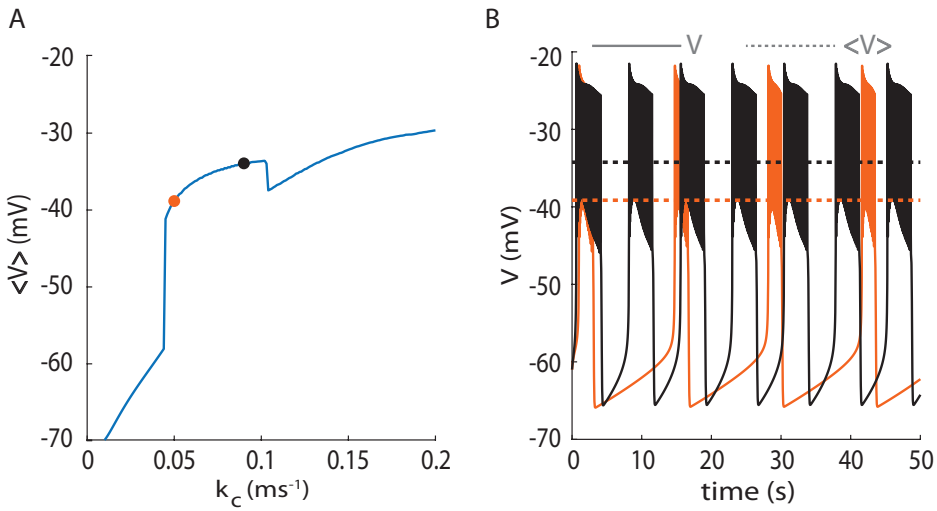

Figure 11. *Lack of dynamic homeostasis in the fast subsystem of the reduced Chay–Keizer model.* (A) *Time-average of V plotted as a function of k_c shows no dynamic homeostasis.* (B) *The time series (solid curves) for $k_c = 0.05$ ms^{-1} (orange) and $k_c = 0.09$ ms^{-1} (black) show that the burst duty cycle is much higher when k_c is larger, raising the time-average of V far above that for the lower k_c value (dashed lines).*

time-average down because the cell spends more time in the silent phase compared to the active phase. The duty cycle is higher with the higher k_c value, producing a higher value of $\langle V \rangle$. The large difference in the duty cycle is responsible for the lack of dynamic homeostasis in the bursting fast subsystem.

3.4. Stochasticity in the Chay–Keizer model extends the range of homeodynamics.

Analogous to adding noise to the input J in the FHN model, we now add noise to the glucose-dependent parameter k_c in the reduced Chay–Keizer model:

$$\frac{dV}{dt} = -(I_{Ca} + I_K + I_{K(Ca)} + I_{K(ATP)} - I_{ap})/C_m, \tag{7}$$

$$\frac{dw}{dt} = \frac{w_\infty(V) - w}{\tau_w}, \tag{8}$$

$$\frac{dc}{dt} = -f(\beta I_{Ca} + k_c^* c), \tag{9}$$

where all variables and parameters are defined as in (4)–(6), except the new calcium pump rate k_c^*, which now follows a folded normal distribution:

$$k_c^* \sim FN(k_c, \sigma). \tag{10}$$

This distribution, a variant of the normal distribution, was used to ensure that the pump rate remains nonnegative. Details of the folded normal distribution are given in Appendix B.

We numerically solved the system (7)–(9) using the forward Euler method, randomly assigning a new calcium pump rate every 1 s according to (10). We then calculated the time-average of the Ca^{2+} concentration, $\langle c \rangle$, after sufficiently long time for many different values

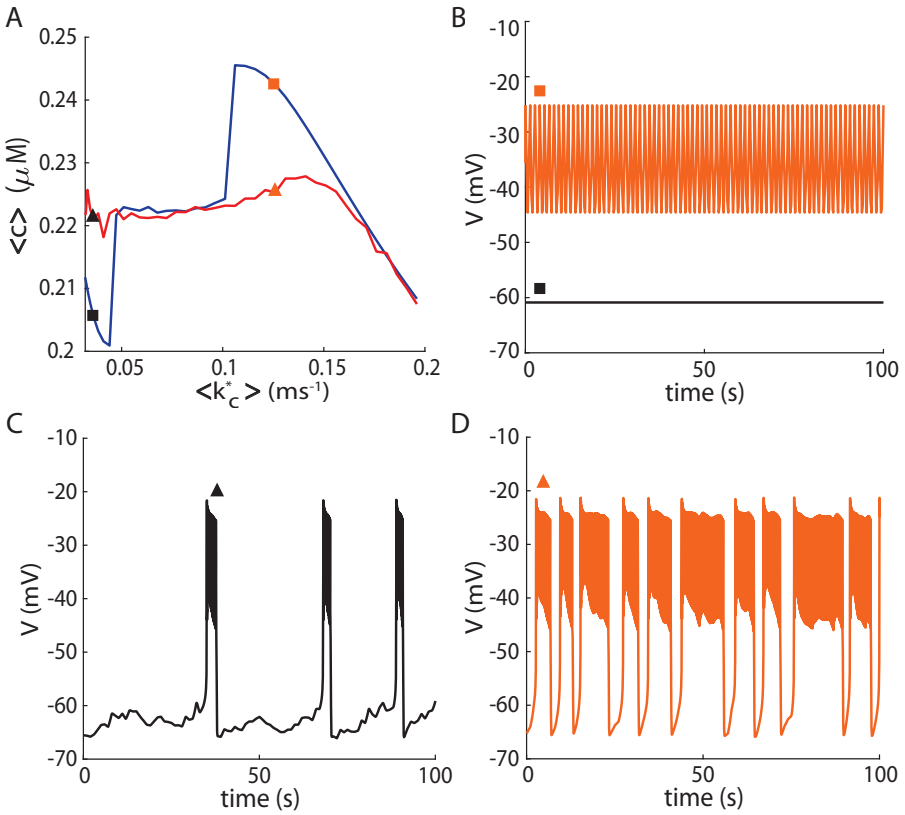

Figure 12. *Dynamic homeostasis is preserved and extended when stochasicity is added to the Ca^{2+} pump rate of the reduced Chay–Keizer model.* (A) *Homeostatic chair curves for the deterministic (blue, $\sigma = 0$) and stochastic (red, $\sigma = 0.04$) versions of the model.* (B) *Membrane potential time series of the deterministic model when $k_c \approx 0.036$ (black square) and $k_c \approx 0.126$ (orange square).* (C) *Membrane potential time series of the stochastic model when $\langle k_c^* \rangle \approx 0.036$ (black triangle).* (D) *Membrane potential time series of stochastic model when $\langle k_c^* \rangle \approx 0.126$ (orange triangle).*

of the folded normal distribution mean, k_c. This is plotted in Figure 12(A) as a function of the expected value of the pump rate, $\langle k_c^* \rangle$ (see Appendix B for the expected value formula for the folded normal distribution). The blue curve corresponds to the deterministic simulation (when $\sigma = 0$), while the red curve is the stochastic simulation (when $\sigma = 0.04$).

For low values of $\langle k_c^* \rangle$, $\langle c \rangle$ for the stochastic model is relatively invariant and has a higher value than in the deterministic case. The reason for this is evident from the V time courses of the stochastic and the deterministic model. For a low value of k_c in the deterministic model (denoted by a black square in Figure 12(A)), the membrane potential is quiescent at a low value (black curve in Figure 12(B)). However, at the same mean value of k_c^* in the stochastic model (black triangle), k_c^* is sampled at some values in which bursting is produced, resulting in an irregular burst pattern (Figure 12(C)). This results in higher Ca^{2+} time-averages.

For intermediate values of $\langle k_c^* \rangle$, the stochastic and deterministic Ca^{2+} time-averages are both semi-invariant, forming the seat of the chair curve. Within this range, both the deterministic and stochastic time series exhibit regular bursting (not shown).

For a high value of $\langle k_c^* \rangle$, the seat of the chair extends considerably farther in the stochastic model than it did in the deterministic model. The reason for this is again evident from an examination of the time series. At a large k_c value, the deterministic model (orange square) produces continuous spiking (orange curve in Figure 12(B)), a behavior in which dynamic homeostasis does not occur. For the stochastic model with the same mean value of k_c (orange triangle), the membrane potential produces periods of regular bursting with moments of extended silent and active phases (see Figure 12(D)). Because the burst pattern is dominant, dynamic homeostasis occurs at and near this value of $\langle k_c^* \rangle$. Also, due to the silent phases between active spiking phases, the mean Ca^{2+} concentration is lower than in the deterministic model.

4. Dynamic homeostasis occurs in bursting oscillations with multiple slow variables. We have shown that dynamic homeostasis can be achieved in the FHN model where a single slow variable drives relaxation oscillations, and in the reduced Chay–Keizer model in which a single slow variable (the Ca^{2+} concentration) drives the bursting oscillations. What happens when there are multiple slow variables? Does dynamic homeostasis still occur, and if so, which of the slow variables maintains semi-invariance in the mean as an input parameter is varied? To address these questions, we studied the phantom bursting model (PBM) for pancreatic β-cells [7, 9].

The PBM is an extension of the reduced Chay–Keizer model with additional dynamics for the Ca^{2+} concentration in the endoplasmic reticulum (ER, denoted as c_{er}) and the ratio of adenosine diphosphate (ADP) to adenosine triphosphate (ATP), $a = \frac{[ADP]}{[ATP]}$. The differential equations for this "phantom bursting model" (PBM) are

$$\begin{aligned}
\frac{dV}{dt} &= -(I_{Ca} + I_K + I_{K(Ca)} + I_{K(ATP)})/C_m, \\
\frac{dw}{dt} &= \frac{w_\infty(V) - w}{\tau_w}, \\
\frac{dc}{dt} &= f_{cyt}(J_{mem} + J_{er}), \\
\frac{c_{er}}{dt} &= -f_{er}(V_{cyt}/V_{er})J_{er}, \\
\frac{da}{dt} &= \frac{a_\infty(c) - a}{\tau_a}.
\end{aligned} \tag{11}$$

The details for the model variables and parameters are discussed in Appendix C. System (11) includes three slow variables (c, c_{er}, and a), and each can independently drive bursting oscillations in the membrane potential depending on the parameters. Of these three, the cytosolic Ca^{2+} concentration c is the fastest, with the ER Ca^{2+} concentration c_{er} varying on a slower timescale. The nucleotide ratio, a, varies on the slowest timescale and is itself a function of c rather than voltage V. These variables are discussed in detail in [9], and a detailed timescale analysis of V, c, and c_{er} was performed in [34]. The timescale for a is simply the constant $\tau_a = 5$ min. It was shown in [9] that when the conductance of the K(Ca) current ($g_{K(Ca)}$) is large any bursting that occurs is fast, with a period of approximately 10 s. This fast bursting is driven entirely or almost entirely by the dynamics of c. If the K(Ca) conductance is small, then the bursting that occurs is slow, with a period of approximately 5 min, and is driven primarily by the dynamics of a.

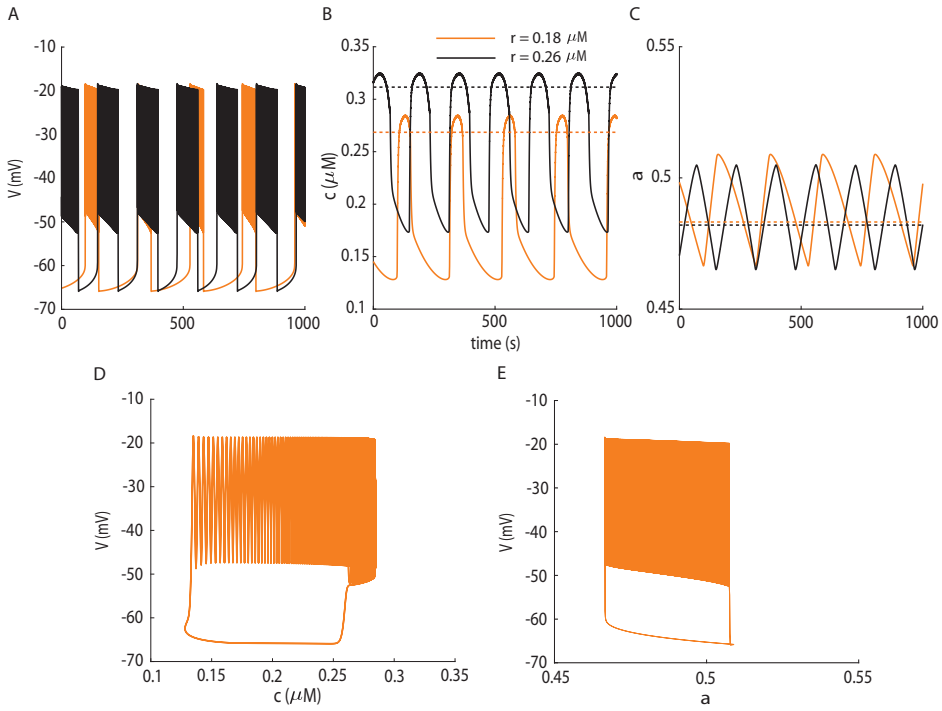

Figure 13. *Dynamic homeostasis in the mean* $\frac{[ADP]}{[ATP]}$ *ratio* a *in the PBM model when* $g_{K(Ca)} = 25$ *pS and bursting is slow. Time series for* (A) *membrane potential,* (B) *cytosolic* Ca^{2+} *concentration, and* (C) $\frac{[ADP]}{[ATP]}$ *ratio when* $r = 0.18$ μM *(orange) and* $r = 0.26$ μM *(black). The time-average of* a *exhibits dynamic homeostasis, but the time-average of* c *does not.* (D) *The burst trajectory in* (c, V)*-space moves to the right during the first part of the burst active phase, and moves back to the left during the second part. Only the case with* $r = 0.18$ μM *is shown here and in the next panel.* (E) *The burst trajectory in* (a, V)*-space, with* a *moving monotonically to the right during the burst active phase, and to the left during the burst silent phase. Other parameters are given in Table 2.*

Figure 13 shows the dynamics of V, c, and a when the Ca^{2+}-activated K^+ maximum conductance is at a low value, $g_{K(Ca)} = 25$ pS. To determine whether this system can display dynamic homeostasis, we varied the metabolism parameter r, which is a parameter in the a differential equation (see Appendix C). Increasing r translates the a-nullcline upward in the (a, V)-plane (not shown), playing a role similar to that played by k_c with c in the reduced Chay–Keizer model. When r is increased from 0.18 μM (orange curves) to 0.26 μM (black curves), there are a decrease in the burst period and an increase in its duty cycle (Figure 13(A)), and for this reason r is considered the glucose-sensing parameter in the model. These changes have a big impact on c, which has a smaller amplitude and considerably larger time-average with the higher r value (Figure 13(B)). In contrast, the time-average of a is almost invariant (Figure 13(C)), indicating dynamic homeostasis in the time-average of this slow variable to changes in the glucose parameter r.

As illustrated in Figure 10, the dynamic homeostasis occurs because the slow variable that drives bursting, i.e., starts and stops active phases of spiking, oscillates over the same range of values when a parameter, like k_c in that case and r in this case, is varied. The active phase starts at a fast-subsystem saddle-node bifurcation and ends when the trajectory

moves past a fast-subsystem homoclinic bifurcation. All that changes is the location of the slow nullcline. We plotted the solution trajectory when $r = 0.18\ \mu M$ in the (c, V)-plane in Figure 13(D). During the silent and much of the active phase, the burst trajectory looks much like it did in Figure 9(B). However, rather than crossing through the fast-subsystem homoclinic bifurcation, the trajectory stalls, and even moves back to the left before the active phase terminates. This indicates that the K(Ca) ionic current activated by c is insufficient to terminate the active phase. It also indicates that c is not driving the bursting. The variable that is driving the bursting is a. When the trajectory is viewed in the (a, V)-plane, it looks just as it did in Figure 9(B), but with a different slow variable. That is, the active phase starts at a fast-subsystem saddle-node bifurcation and ends at a fast-subsystem homoclinic bifurcation (the fast-subsystem would be the variables other than a); a is driving the bursting in this case. This projection of the trajectory looks the same for the two values of parameter r and explains the dynamic homeostasis in the time-average of a.

Figure 14 shows the dynamics of V, c, and a when the Ca^{2+}-activated K^+ maximum conductance is large, $g_{K(Ca)} = 600$ pS. Since bursting is now driven by c, we varied a parameter

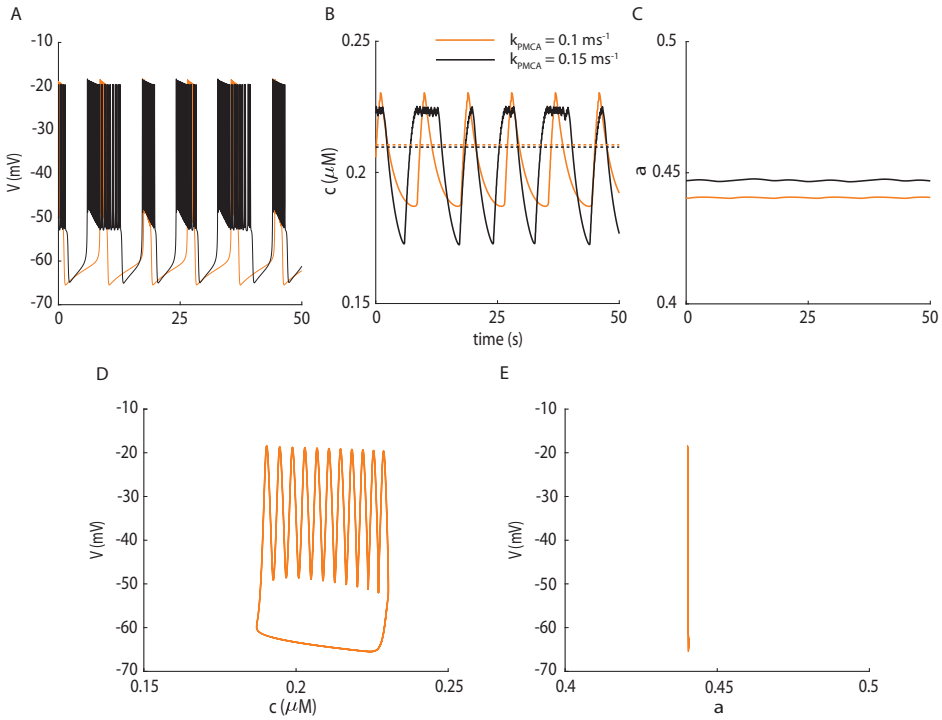

Figure 14. *Dynamic homeostasis in the mean cytosolic Ca^{2+} concentration c in the PBM model when $g_{K(Ca)} = 600$ pS. Time series for* (A) *membrane potential,* (B) *cytosolic Ca^{2+} concentration, and* (C) $\frac{[ADP]}{[ATP]}$ *ratio when $k_{PMCA} = 0.1\ ms^{-1}$ (orange) and $k_{PMCA} = 0.15\ ms^{-1}$ (black).* (D) *The burst trajectory projected into the (c, V)-plane moves to the right during the active phase and to the left during the silent phase, having a profile typical for a variable that drives bursting. Only the case with $k_{PMCA} = 0.1\ ms^{-1}$ is shown here and in the next panel.* (E) *The projection of the burst trajectory into the (a, V)-plane appears as a vertical line segment since a is relatively constant during this fast bursting and plays no role in driving the bursting. Other parameters are given in Table 2.*

in the c differential equation, the Ca^{2+} pump rate k_{PMCA} (called k_c in the Chay–Keizer model). When k_{PMCA} was raised from 0.1 ms^{-1} (orange curves) to 0.15 ms^{-1} (black curves), the burst duty cycle increased, similar to before in the Chay–Keizer model. Unlike in Figure 13, dynamic homeostasis was present in the time-average of c (see Figure 14(B)). The time-average of a was not invariant, but increased with k_{PMCA} (see Figure 14(C)). From the projection of the burst trajectory into the (c, V)-plane (Figure 14(D)), it is apparent that the bursting is driven by c, just as with the Chay–Keizer model in Figure 9(B). In contrast, the trajectory projected into the (a, V)-plane (Figure 14(E)) shows that a is almost constant during this fast bursting and plays no role in driving the burst.

The central conclusion from this analysis is that dynamic homeostasis is present in a bursting model with multiple slow variables, but only in the slow variable that drives the bursting oscillations.

5. Discussion. Homeostasis is a fundamental principle in biology, and much recent work has been done on understanding it from a dynamical systems viewpoint in signaling pathways [39, 40, 41]. The focus there was on the semi-invariance of a system variable at static equilibrium in response to change in input. Other works [31, 56] have argued for the reemergence of a more general approach to homeostasis, the concept of dynamic homeostasis. Real biological systems are complex with many degrees of freedom allowing for more complicated outputs like bistability, oscillations, chaos, or possibly some combination. Everyone has heard how normal body temperature is 98.6°F (37°C) or that normal blood glucose level is about 85 mg/dL (4.7 mmol/L). However, these are only averages. Body temperature [2], glucose, and insulin [51] all oscillate over time even with constant, controlled conditions present.

In this article, we demonstrated that homeostasis can occur even in oscillatory systems. In particular, this dynamic homeostasis occurs in oscillatory systems with fast-slow dynamics such as relaxation oscillations and electrical bursting oscillations. We also demonstrated that the homeostasis is restricted to the slow variable that drives the oscillation; fast variables do not exhibit the behavior, nor do additional slow variables not responsible for driving oscillations. This modeling form for dynamic homeostasis requires the input parameter to modulate the same variable that encodes homeostasis. Other forms of dynamic homeostasis may exist where the input and output relate to different variables. The dynamic homeostasis is robust to noise in the input to the slow subsystem, and in fact this type of noise can extend the range of input at which dynamic homeostasis occurs. This is one of many ways stochasticity can be implemented in the models. For example, noise could be introduced into the fast subsystem, it could affect a different parameter besides the input, it could affect multiple parameters simultaneously, or a different sampling distribution could be used.

What advantage might there be to a cell to maintain a constant average level of a slow variable over a range of inputs? Of course, this depends on the slow variable. For the Chay–Keizer model, there is semi-invariance in the mean cytosolic Ca^{2+}. This could be desirable as a means to ensure that the Ca^{2+} level does not go too high even as the variable's production is increased. This ion regulates many enzymes and transcription factors, and some ion channels. It is also a trigger for secretion, as we discuss below. Programmed cell death, apoptosis, is also triggered by sustained Ca^{2+} levels in the cytoplasm and mitochondria of a cell. Therefore,

the intracellular Ca^{2+} level should be tightly regulated, and dynamic homeostasis as in the Chay–Keizer model is one way to achieve this. Likewise, creatine kinase is found in many tissues and acts as an ATP buffer, storing ATP for future use if needed. The dynamic homeostasis of the mean $\frac{[ADP]}{[ATP]}$ level is another means for keeping the nucleotide ratio constant even as the production of ATP from ADP is increased. In ecological systems, the birth/death dynamics of predator and prey can vary substantially, giving rise to population dynamics with fast and slow subsystems. This is true, for example, in resource-consumer interactions, where the life cycle of the consumer (e.g., insect herbivores) can be much shorter than that of the resource (the trees that they feed on). Such systems can exhibit relaxation oscillations [24], and while the resource level may oscillate over time, its average value would be homeostatic over a large range of parameter values in its subsystem.

The two models for bursting used in this article were developed to describe bursting in β-cells from pancreatic islets of Langerhans. These cells secrete insulin in response to the blood glucose level; higher glucose levels, as would occur after a meal, result in higher insulin secretion. Therefore, the primary input to these cells is glucose and the primary output is insulin. The transduction pathway between input and output is very complicated [46, 47] and has been the focus of mathematical modeling since 1983 with the publication of the Chay–Keizer model [12]. In that original model, the input (glucose) acted directly on the Ca^{2+} pump rate, k_c, since the product of glucose metabolism in the cell, ATP, powers those pumps. Although a very sensible notion, we have shown here that with that model and that source of input, the temporal average level of Ca^{2+} is almost constant over the entire range of input values for which the cell is bursting (the state of the cell when the animal is in a fed state). Since insulin secretion is evoked by the binding of Ca^{2+} to proteins in the exocytotic machinery, this would lead to a relatively steady level of insulin secretion at all stimulatory glucose levels if the relationship between Ca^{2+} concentration and insulin were linear. The reality is much more complicated than that [48], but an invariant average Ca^{2+} level with changes in glucose is nonetheless a very undesirable feature, and is a byproduct of the key role that the Ca^{2+} concentration plays in driving bursting in that model.

In the phantom bursting model used in the latter part of this study, the role of burst driver during the slow bursting typically observed in islets is played by a different variable, a, the ratio of ADP to ATP in the cell. This ratio sets the activation level of ATP-sensitive K^+ channels, K(ATP) channels, which were not discovered until after the publication of the Chay–Keizer model [3, 13, 25]. Since $a = \frac{[\mathrm{ADP}]}{[\mathrm{ATP}]}$ now drives the bursting, the cytosolic Ca^{2+} concentration is released from homeostasis, so it can, and does, increase with higher glucose concentrations. This is much more appropriate for β-cell function. Thus, dynamic homeostasis of the nucleotide ratio may simply be a byproduct of a design that aims to have increased insulin secretion with higher levels of blood glucose. The semi-invariance in the nucleotide ratio in β-cell models in which bursting is driven by the nucleotide ratio was first described in [33] and was supported by experimental data in the same publication. This fact was used to make the case that slow bursting in these cells was driven by oscillations in the K(ATP) channel conductance, rather than through K(Ca) conductance. A much earlier study recognized the semi-invariance of the cytosolic Ca^{2+} concentration in a model where bursting was driven by Ca^{2+} through actions on K(Ca) channels [26].

What this study adds to these prior studies is a demonstration of the persistence of this phenomenon across oscillators with a fast-slow structure, and the robustness of the phenomenon to noise. Also, the manner in which the dynamic homeostasis manifests in systems with multiple slow variables was described here for the first time. In particular, we demonstrated that it is only the slow variable responsible for driving bursting that exhibits dynamic homeostasis. This generalizes naturally to relaxation oscillators with multiple slow variables. In addition, our analysis suggests an experimental approach for determining which biological variable is responsible for driving bursting oscillations. Slow variables that do not exhibit dynamic homeostasis in response to changes in the input to that subsystem are not drivers of the oscillations. The slow variable that does exhibit dynamic homeostasis is the one driving the oscillation. This would be good to know even if no mathematical model has yet been developed; the different potential slow variables could be measured (if possible) and checked for invariance of the mean. This could help identify which variable drives the oscillation and could be the basis for subsequent model development.

Appendix A. Linear stability analysis and Hopf bifurcation for the FHN model. In this appendix, we linearize the FHN model to find equations for Hopf bifurcations of the FHN model. The elements of the vector field for the FHN model are

$$g(x,y)=\mu\left(x-\frac{x^3}{3}-y\right), \qquad h(x,y)=\frac{1}{\mu}(J+\alpha x-y),$$

where an equilibrium (x^*,y^*) satisfies $g(x^*,y^*)=h(x^*,y^*)=0$, or

$$\frac{x^{*3}}{3}+(\alpha-1)x^*+J=0, \qquad y^*=J+\alpha x^*.$$

The Jacobian for the linearized system is

$$A=\begin{pmatrix}\mu(1-x^{*2}) & -\mu\\ \frac{\alpha}{\mu} & -\frac{1}{\mu}\end{pmatrix},$$

where the trace and determinant are $T=\mu(1-x^{*2})-\frac{1}{\mu}$ and $D=x^{*2}+\alpha-1$. A saddle-node bifurcation occurs when there is one zero eigenvalue and one nonzero eigenvalue, so $D=0$ and $T\neq 0$. This occurs at $\alpha=1$ and $x^*=0$. For $\alpha<1$ there are three equilibria, while for $\alpha>1$ there is a single equilibrium. We consider only the latter case in this study.

A Hopf bifurcation occurs when the eigenvalues of the Jacobian are purely imaginary, so $T=0$ and $D\neq 0$. These conditions give the locations and conditions for a Hopf bifurcation in terms of the parameters

$$\begin{aligned} x^*_{\pm}&=\pm\sqrt{1-\frac{1}{\mu^2}},\\ J_{\pm}&=\pm(1-\alpha)\left(1-\frac{1}{\mu^2}\right)^{\frac{1}{2}}\mp\frac{1}{3}\left(1-\frac{1}{\mu^2}\right)^{\frac{3}{2}},\\ \alpha&>\frac{1}{\mu^2}. \end{aligned} \tag{12}$$

In this manuscript, we assume $\mu \gg 1$ to ensure a large timescale separation between the x and y species, and since we only consider the case $\alpha > 1$ the last condition is always satisfied. Given $\mu \gg 1$ we can approximate the Hopf bifurcation curves in (12) as $J_\pm \approx \pm(\frac{2}{3} - \alpha)$. The Hopf bifurcation curves are shown in a two-parameter bifurcation diagram in Figure 6(C). For $\frac{2}{3} - \alpha < J < \alpha - \frac{2}{3}$, the equilibrium is unstable and stable periodic solutions can exist. Otherwise, the equilibrium is locally stable and no periodic solutions exist.

Appendix B. The folded normal distribution. The folded normal distribution was used in the stochastic Chay–Keizer model to ensure the Ca^{2+} pump rate, k_c, remained nonnegative during simulations. Given a normally distributed random variable X with mean k_c and standard deviation σ, the random variable $k_c^* = |X|$ has a folded normal distribution. The transformed expected value and standard deviation are as follows:

$$\begin{aligned} \langle k_c^* \rangle &= \sqrt{\frac{2}{\pi}}\sigma \exp\left(-\frac{k_c^2}{2\sigma^2}\right) + \mu\left(1 - 2\Phi\left(-\frac{k_c}{\sigma}\right)\right), \\ \sigma_f &= \sqrt{k_c^2 + \sigma^2 - \langle k_c^* \rangle^2}, \end{aligned} \tag{13}$$

where $\Phi(x) = \frac{1}{2}(1 - \mathrm{erf}(\frac{x}{\sqrt{2}}))$ is the normal cumulative distribution function. The function $\mathrm{erf}(z) = \frac{2}{\sqrt{\pi}} \int_0^z e^{-t^2} dt$ is the Gauss error function.

Appendix C. The phantom bursting model. The phantom bursting model (PBM) is a pancreatic cell model first introduced and analyzed in [7]. The model includes the dynamics of five variables as follows:

$$\begin{aligned} \frac{dV}{dt} &= -(I_{Ca} + I_K + I_{K(Ca)} + I_{K(ATP)})/C_m, \\ \frac{dw}{dt} &= \frac{w_\infty(V) - w}{\tau_w}, \\ \frac{dc}{dt} &= f_{cyt}(J_{mem} + J_{er}), \\ \frac{c_{er}}{dt} &= -f_{er}(V_{cyt}/V_{er})J_{er}, \\ \frac{da}{dt} &= \frac{a_\infty(c) - a}{\tau_a}, \end{aligned}$$

where V is the membrane potential, w is the delayed rectifier activation, c is the free cytosolic Ca^{2+} concentration, c_{er} is the free Ca^{2+} concentration in the endoplasmic reticulum (ER), and a is the nucleotide ratio ($\frac{[ADP]}{[ATP]}$). The parameters used in this model are given in Table 2.

The dynamics of the membrane potential V are governed by the different ionic currents and by the membrane capacitance C_m. The ionic current are given by

$$\begin{aligned} I_{Ca} &= g_{Ca} m_\infty(V)(V - V_{Ca}), \\ I_K &= g_K w(V - V_K), \\ I_{K(Ca)} &= g_{K(Ca)} \frac{c^5}{K_d^5 + c^5}(V - V_K), \\ I_{K(ATP)} &= g_{K(ATP)} a(V - V_K). \end{aligned}$$

Table 2

Parameter values used in all figures for the PBM, except k_{PMCA}, r, and $g_{K(Ca)}$ which are varied from their default values in Figures 13 and 14.

Parameter	Value	Parameter	Value
g_{Ca}	1200 pS	r	0.225 μM
$g_{K(Ca)}$	600 pS	V_{cyt}/V_{er}	10
g_K	3000 pS	K_d	0.4 μM
$g_{K(ATP)}$	500 pS	τ_w	18 ms
C_m	5300 fF	τ_a	300,000 ms
v_w	-15 mV	s_w	5 mV
v_m	-20 mV	s_m	12 mV
p_{leak}	0.0002 ms^{-1}	s_a	0.1 μM
V_K	-75 mV	f_{cyt}	0.001
V_{Ca}	25 mV	f_{er}	0.01
SERCA$_3$	0.2 ms^{-1}	SERCA$_{2b}$	0.02 μM ms^{-1}
β	$4.5 \times 10^{-6}\mu$M fA^{-1} ms^{-1}	k_{PMCA}	0.125 ms^{-1}

The equilibrium activation functions are increasing Boltzmann functions:

$$m_\infty(V) = \frac{1}{1+\exp\left(\frac{v_m - V}{s_m}\right)},$$
$$w_\infty(V) = \frac{1}{1+\exp\left(\frac{v_w - V}{s_w}\right)},$$
$$a_\infty(c) = \frac{1}{1+\exp\left(\frac{r - c}{s_a}\right)}.$$

The last of these, for $a_\infty(c)$, contains the parameter r that is varied in Figure 13. Increasing r shifts the sigmoidal curve to the right.

The flux of Ca^{2+} through the membrane is

$$J_{mem} = -(\beta I_{Ca} + k_{PMCA} c),$$

where β converts units of current to flux, and $k_{PMCA}c$ is the flux through the plasma membrane Ca^{2+} pumps. The parameter k_{PMCA} is varied in Figure 14. We assume the Ca^{2+} influx into the ER occurs via sarcoplasmic endoplasmic reticulum Ca^{2+} (SERCA) pumps with high (SERCA$_{2b}$) and lower affinity (SERCA$_3$):

$$J_{\text{SERCA}} = \text{SERCA}_{2b} + \text{SERCA}_3 c.$$

The efflux out of the ER is the Ca^{2+} leak, which is taken to be proportional to the gradient difference between Ca^{2+} in the cytosol and the ER:

$$J_{leak} = p_{leak}(c_{er} - c).$$

The net Ca^{2+} efflux from the ER is

$$J_{er} = J_{leak} - J_{\text{SERCA}}.$$

The c differential equation is then the sum of membrane and ER fluxes multiplied by the fraction of free total Ca^{2+}, f_{cyt}.

For the ER Ca^{2+}, J_{er} is scaled by the ratio of the volumes of the cytoplasmic compartment (V_{cyt}) and the ER compartment (V_{er}) and multiplied by the fraction of free Ca^{2+} in the ER (f_{er}) giving the differential equation for c_{er}.

Appendix D. Further reading. *Homeostasis* [15, 23, 39, 40, 41].
Dynamic homeostasis [31, 56, 57].
Relaxation oscillations [8, 24].
Bursting oscillations [5, 6, 7, 9, 14, 42, 43, 44, 45, 52].

Author declarations and contributions. The authors declare that they have no conflicts of interest.

RB and BRK conceptualized the work. CJR performed all mathematical analysis and numerical simulations and wrote the original draft of the manuscript. RB and BRK administered the project and acquired funding. All authors wrote and edited later drafts.

Data availability. All code for reproducing the figures in this manuscript is available at https://cryzowicz.wixsite.com/chris-ryzowicz/general-5.

REFERENCES

[1] R. J. Alpern, R. Belitsky, and S. Long, *Competencies in premedical and medical education: The AAMC–HHMI Report*, Perspect. Biol. Med., 54 (2011), pp. 30–35, 10.1353/pbm.2011.0001.
[2] J. Aschoff, M. Fatranska, H. Giedke, P. Doerr, D. Stamm, and H. Wisser, *Human circadian rhythms in continuous darkness: Entrainment by social cues*, Science, 171 (1971), pp. 213–215, 10.1126/science.171.3967.213.
[3] F. M. Ashcroft, D. E. Harrison, and S. J. H. Ashcroft, *Glucose induces closure of single potassium channels in isolated rat pancreatic β-cells*, Nature, 312 (1984), pp. 446–448, https://www.nature.com/articles/312446a0.
[4] I. Atwater, C. Dawson, A. Scott, G. Eddlestone, and E. Rojas, *The nature of the oscillatory behaviour in electrical activity from pancreatic beta-cell*, Horm. Metab. Res. Suppl., (1980), pp. 100–107, https://europepmc.org/article/med/7005051.
[5] R. Bertram, M. J. Butte, T. Kiemel, and A. Sherman, *Topological and phenomenological classification of bursting oscillations*, Bull. Math. Biol., 57 (1995), pp. 413–439, 10.1007/BF02460633.
[6] R. Bertram, I. Marinelli, P. A. Fletcher, L. S. Satin, and A. S. Sherman, *Deconstructing the integrated oscillator model for pancreatic β-cells*, Math. Biosci., 365 (2023), 109085, https://doi.org/10.1016/j.mbs.2023.109085.
[7] R. Bertram, J. Previte, A. Sherman, T. A. Kinard, and L. S. Satin, *The phantom burster model for pancreatic β-cells*, Biophys. J., 79 (2000), pp. 2880–2892, https://doi.org/10.1016/S0006-3495(00)76525-8.
[8] R. Bertram and J. E. Rubin, *Multi-timescale systems and fast-slow analysis*, Math. Biosci., 287 (2017), pp. 105–121, 10.1016/j.mbs.2016.07.003.
[9] R. Bertram and A. Sherman, *A calcium-based phantom bursting model for pancreatic islets*, Bull. Math. Biol., 66 (2004), pp. 1313–1344, 10.1016/j.bulm.2003.12.005.
[10] J. Best, A. Borisyuk, J. Rubin, D. Terman, and M. Wechselberger, *The dynamic range of bursting in a model respiratory pacemaker network*, SIAM J. Appl. Dyn. Syst., 4 (2005), pp. 1107–1139, https://doi.org/10.1137/050625540.
[11] P. C. Bressloff, *Stochastic Processes in Cell Biology*, Interdiscip. Appl. Math. 41, Springer, Cham, 2014.
[12] T. R. Chay and J. Keizer, *Minimal model for membrane oscillations in the pancreatic β-cell*, Biophys. J., 42 (1983), pp. 181–189, 10.1016/S0006-3495(83)84384-7.

[13] D. L. Cook and N. Hales, *Intracellular ATP directly blocks K^+ channels in pancreatic B-cells*, Nature, 311 (1984), pp. 271–273, 10.1038/311271a0.
[14] M. Desroches, J. Rinzel, and S. Rodrigues, *Classification of bursting patterns: A tale of two ducks*, PLoS Comput. Biol., 18 (2022), e1009752, https://doi.org/10.1371/journal.pcbi.1009752.
[15] W. Duncan, J. Best, M. Golubitsky, H. Nijhout, and M. Reed, *Homeostasis despite instability*, Math. Biosci., 300 (2018), pp. 130–137, 10.1016/j.mbs.2018.03.025.
[16] W. Duncan and M. Golubitsky, *Coincidence of homeostasis and bifurcation in feedforward networks*, Internat. J. Bifur. Chaos Appl. Sci. Engrg., 29 (2019), 1930037, https://doi.org/10.1142/S0218127419300374.
[17] R. FitzHugh, *Impulses and physiological states in theoretical models of nerve membrane*, Biophys. J., 1 (1961), pp. 445–466, 10.1016/s0006-3495(61)86902-6.
[18] R. FitzHugh, *Mathematical models of excitation and propagation in nerve*, Biol. Eng., 9 (1969), pp. 1–85.
[19] P. C. Franzone, P. Deuflhard, B. Erdmann, J. Lang, and L. F. Pavarino, *Adaptivity in space and time for reaction-diffusion systems in electrocardiology*, SIAM J. Sci. Comput., 28 (2006), pp. 942–962, https://doi.org/10.1137/050634785.
[20] M. Golubitsky and I. Stewart, *Homeostasis, singularities, and networks*, J. Math. Biol., 74 (2017), pp. 387–407, https://doi.org/10.1007/s00285-016-1024-2.
[21] M. Golubitsky and I. Stewart, *Homeostasis with multiple inputs*, SIAM J. Appl. Dyn. Syst., 17 (2018), pp. 1816–1832, https://doi.org/10.1137/17M115147X.
[22] M. Golubitsky, I. Stewart, F. Antoneli, Z. Huang, and Y. Wang, *Input-output networks, singularity theory, and homeostasis*, in Advances in Dynamics, Optimization and Computation: A Volume Dedicated to Michael Dellnitz on the Occasion of his 60th Birthday, Springer, 2020, pp. 31–65.
[23] A. C. Guyton and J. E. Hall, *Guyton and Hall Textbook of Medical Physiology*, Elsevier Saunders, Pennsylvania, 2006.
[24] A. Hastings, K. C. Abbott, K. Cuddington, T. Francis, G. Gellner, Y.-C. Lai, A. Morozov, S. Petrovskii, K. Scranton, and M. L. Zeeman, *Transient phenomena in ecology,* Science, 361 (2018), eaat6412, https://doi.org/10.1126/science.aat6412.
[25] J.-C. Henquin, *ATP-sensitive K^+ channels may control glucose-induced electrical activity in pancreatic B-cells*, Biochem. Biophys. Res. Commun., 156 (1988), pp. 769–775, https://doi.org/10.1016/S0006-291X(88)80910-0.
[26] D. M. Himmel and T. R. Chay, *Theoretical studies on the electrical activity of pancreatic β-cells as a function of glucose*, Biophys. J., 51 (1987), pp. 89–107, https://doi.org/10.1016/S0006-3495(87)83314-3.
[27] A. L. Hodgkin and A. F. Huxley, *A quantitative description of membrane current and its application to conduction and excitation in nerve*, J. Physiol., 117 (1952), pp. 500–544, https://doi.org/10.1113/jphysiol.1952.sp004764.
[28] E. M. Izhikevich, *Neural excitability, spiking and bursting*, Internat. J. Bifur. Chaos Appl. Sci. Engrg., 10 (2000), pp. 1171–1266, https://doi.org/10.1142/S0218127400000840.
[29] M. Kaern, T. C. Elston, W. J. Blake, and J. J. Collins, *Stochasticity in gene expression: From theories to phenotypes*, Nat. Rev. Genet., 6 (2005), pp. 451–464, https://doi.org/10.1038/nrg1615.
[30] B. Karamched, G. Hripcsak, D. Albers, and W. Ott, *Delay-induced uncertainty for a paradigmatic glucose–insulin model*, Chaos, 31 (2021), 023142, https://doi.org/10.1063/5.0027682.
[31] D. Lloyd, M. A. Aon, and S. Cortassa, *Why homeodynamics, not homeostasis?*, Sci. World J., 1 (2001), pp. 133–145, https://doi.org/10.1100/tsw.2001.20.
[32] R. Losick and C. Desplan, *Stochasticity and cell fate*, Science, 320 (2008), pp. 65–68, https://doi.org/10.1126/science.1147888.
[33] I. Marinelli, B. M. Thompson, V. S. Parekh, P. A. Fletcher, L. Gerardo-Giorda, A. S. Sherman, L. S. Satin, and R. Bertram, *Oscillations in K(ATP) conductance drive slow calcium oscillations in pancreatic β-cells*, Biophys. J., 121 (2022), pp. 1449–1464, https://doi.org/10.1016/j.bpj.2022.03.015.
[34] J. P. McKenna and R. Bertram, *Fast-slow analysis of the Integrated Oscillator Model for pancreatic β-cells*, J. Theoret. Biol., 457 (2018), pp. 152–162, https://doi.org/10.1016/j.jtbi.2018.08.029.

[35] J. Michael, *Conceptual assessment in the biological sciences: A National Science Foundation–sponsored workshop*, Adv. Physiol. Educ., 31 (2007), pp. 389–391, https://doi.org/10.1152/advan.00047.2007.
[36] H. Modell, W. Cliff, J. Michael, J. McFarland, M. P. Wenderoth, and A. Wright, *A physiologist's view of homeostasis*, Adv. Physiol. Edu., 39 (2015), pp. 259–266, https://doi.org/10.1152/advan.00107.2015.
[37] C. Morris and H. Lecar, *Voltage oscillations in the barnacle giant muscle fiber*, Biophys. J., 35 (1981), pp. 193–213, https://doi.org/10.1016/S0006-3495(81)84782-0.
[38] J. Nagumo, S. Arimoto, and S. Yoshizawa, *An active pulse transmission line simulating nerve axon*, Proc. IRE, 50 (1962), pp. 2061–2070, https://doi.org/10.1109/JRPROC.1962.288235.
[39] H. F. Nijhout, J. Best, and M. C. Reed, *Escape from homeostasis*, Math. Biosci., 257 (2014), pp. 104–110, https://doi.org/10.1016/j.mbs.2014.08.015.
[40] H. F. Nijhout, J. A. Best, and M. C. Reed, *Systems biology of robustness and homeostatic mechanisms*, Wiley Interdiscip. Rev. Syst. Biol. Med., 11 (2019), e1440, https://doi.org/10.1002/wsbm.1440.
[41] M. Reed, J. Best, M. Golubitsky, I. Stewart, and H. F. Nijhout, *Analysis of homeostatic mechanisms in biochemical networks*, Bull. Math. Biol., 79 (2017), pp. 2534–2557, https://doi.org/10.1007/s11538-017-0340-z.
[42] J. Rinzel, *A formal classification of bursting mechanisms in excitable systems*, in Mathematical Topics in Population Biology, Morphogenesis and Neurosciences: Proceedings of an International Symposium held in Kyoto, Springer, 1985, pp. 267–281.
[43] J. Rinzel and G. B. Ermentrout, *Analysis of neural excitability and oscillations*, in Methods in Neuronal Modeling: From Synapses to Networks, Vol. 2, C. Koch and I. Segev, eds., MIT Press, Cambridge, 1998, pp. 251–292.
[44] J. Rinzel and Y. S. Lee, *On different mechanisms for membrane potential bursting*, in Nonlinear Oscillations in Biology and Chemistry (Salt Lake City, Utah, 1985), Lecture Notes in Biomath. 66, Springer-Verlag, Berlin, 1986, pp. 19–33.
[45] J. Rinzel and Y. S. Lee, *Dissection of a model for neuronal parabolic bursting*, J. Math. Biol., 25 (1987), pp. 653–675, https://doi.org/10.1007/BF00275501.
[46] P. Rorsman and F. M. Ashcroft, *Pancreatic β-cell electrical activity and insulin secretion: Of mice and men*, Physiol. Rev., 98 (2018), pp. 117–214, https://doi.org/10.1152/physrev.00008.2017.
[47] L. S. Satin, P. C. Butler, J. Ha, and A. S. Sherman, *Pulsatile insulin secretion, impaired glucose tolerance and type 2 diabetes*, Mol. Aspects Med., 42 (2015), pp. 61–77, https://doi.org/10.1016/j.mam.2015.01.003.
[48] A. R. Sedaghat, A. Sherman, and M. J. Quon, *A mathematical model of metabolic insulin signaling pathways*, Amer. J. Physiol., 283 (2002), pp. E1084–E1101, https://doi.org/10.1152/ajpendo.00571.2001.
[49] J. Sneyd, J. M. Han, L. Wang, J. Chen, X. Yang, A. Tanimura, M. J. Sanderson, V. Kirk, and D. I. Yule, *On the dynamical structure of calcium oscillations*, Proc. Natl. Acad. Sci., 114 (2017), pp. 1456–1461, https://doi.org/10.1073/pnas.1614613114.
[50] H. Soodak and A. Iberall, *Homeokinetics: A physical science for complex systems*, Science, 201 (1978), pp. 579–582, https://doi.org/10.1126/science.201.4356.579.
[51] J. Sturis, K. S. Polonsky, E. Mosekilde, and E. Van Cauter, *Computer model for mechanisms underlying ultradian oscillations of insulin and glucose*, Amer. J. Physiol., 260 (1991), pp. E801–E809, https://doi.org/10.1152/ajpendo.1991.260.5.E801.
[52] D. Terman, *The transition from bursting to continuous spiking in excitable membrane models*, J. Nonlinear Sci., 2 (1992), pp. 135–182, https://doi.org/10.1007/BF02429854.
[53] L. S. Tsimring, *Noise in biology*, Rep. Prog. Phys., 77 (2014), 026601, https://doi.org/10.1088/0034-4885/77/2/026601.
[54] B. van der Pol, VII. *Forced oscillations in a circuit with non-linear resistance. (Reception with reactive triode)*, Philos. Mag. (7), 3 (1927), pp. 65–80, https://doi.org/10.1080/14786440108564176.
[55] Y. Wang, Z. Huang, F. Antoneli, and M. Golubitsky, *The structure of infinitesimal homeostasis in input–output networks*, J. Math. Biol., 82 (2021), 62, https://doi.org/10.1007/s00285-021-01614-1.

[56] L. Xiong and A. Garfinkel, *Are physiological oscillations physiological?*, J. Physiol., (2023), https://doi.org/10.1113/JP285015.

[57] F. E. Yates, *Order and complexity in dynamical systems: Homeodynamics as a generalized mechanics for biology*, Math. Comput. Model., 19 (1994), pp. 49–74, https://doi.org/10.1016/0895-7177(94)90189-9.